Electronic Supplementary Material (ESI) for Energy & Environmental Science.

Supporting Information

Co-intercalation-free Ether Electrolytes for Graphitic Anodes in Lithium-ion Batteries

Peiyuan Ma,[1] Priyadarshini Mirmira,[1] Peter J. Eng[3,4], Seoung-Bum Son[2], Ira D. Bloom[2],
Alexander S. Filatov[5] and Chibueze V. Amanchukwu[1*]

[1]Pritzker School of Molecular Engineering, University of Chicago, Chicago, IL 60637, USA

[2]Chemical Sciences and Engineering Division, Argonne National Laboratory, Lemont, IL 60439 USA

[3]Consortium for Advanced Radiation Sources, University of Chicago, Chicago, IL 60637, USA

[4]James Franck Institute, University of Chicago, Chicago, IL 60637, USA.

[5]Department of Chemistry, University of Chicago, Chicago, IL 60637, USA

*Corresponding author

Email: chibueze@uchicago.edu

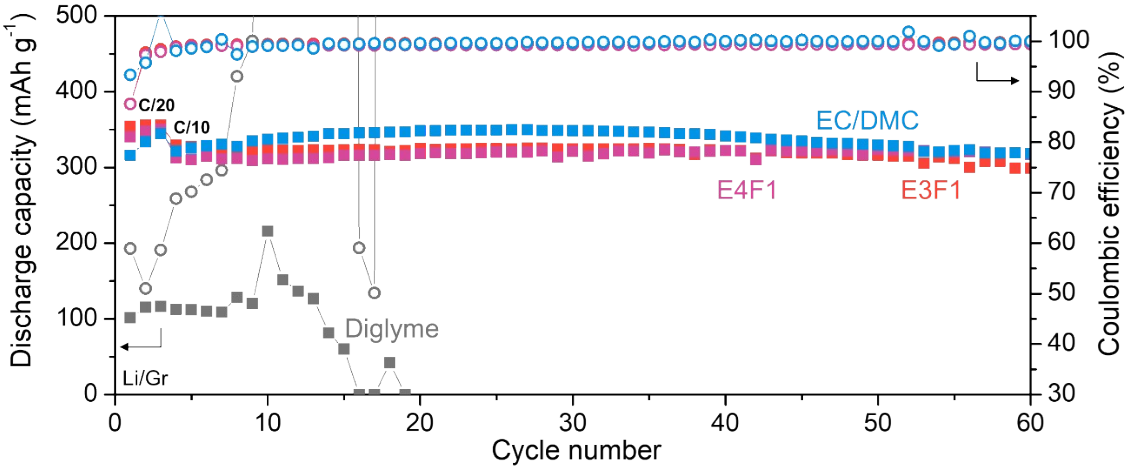

Figure S1. Long term cycling of lithium metal/graphite (Li/Gr) cells using 1 M LiFSA in E3F1, 1 M LiFSA in E4F1, 1 M LiFSA in diglyme and 1 M $LiPF_6$ in EC/DMC. The cells were cycled at a current rate of C/10 after three formation cycles at C/20. (1 C ≈ 2.17 mA cm^{-2})

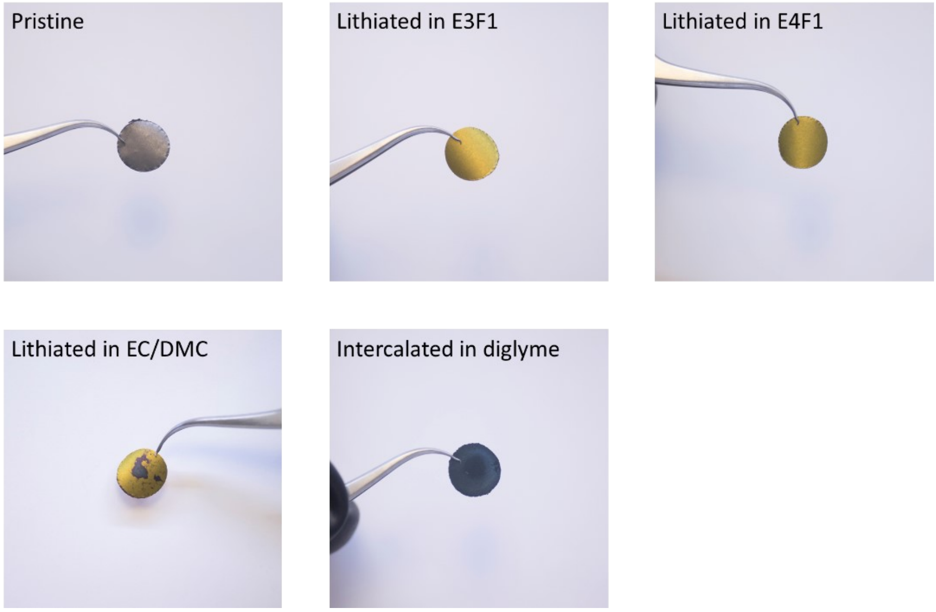

Figure S2. Digital photos of graphite electrode intercalated in different electrolytes with pristine graphite for comparison. The graphite lithiated in E3F1 and E4F1 electrolytes exhibit golden color, corresponding to Li_xC_6 GICs. Graphite lithiated in EC/DMC electrolyte also has golden color despite some defects. However, no such golden color is observed on graphite intercalated in diglyme electrolyte, which indicates the formation of diglyme-lithium-graphite ternary GICs instead of Li_xC_6 complexes. Intercalated graphite electrodes were retrieved from Li/Gr cells intercalated to 0.01 V at a rate of C/20 (1 C $\approx$ 2.17 mA cm^{-2}).

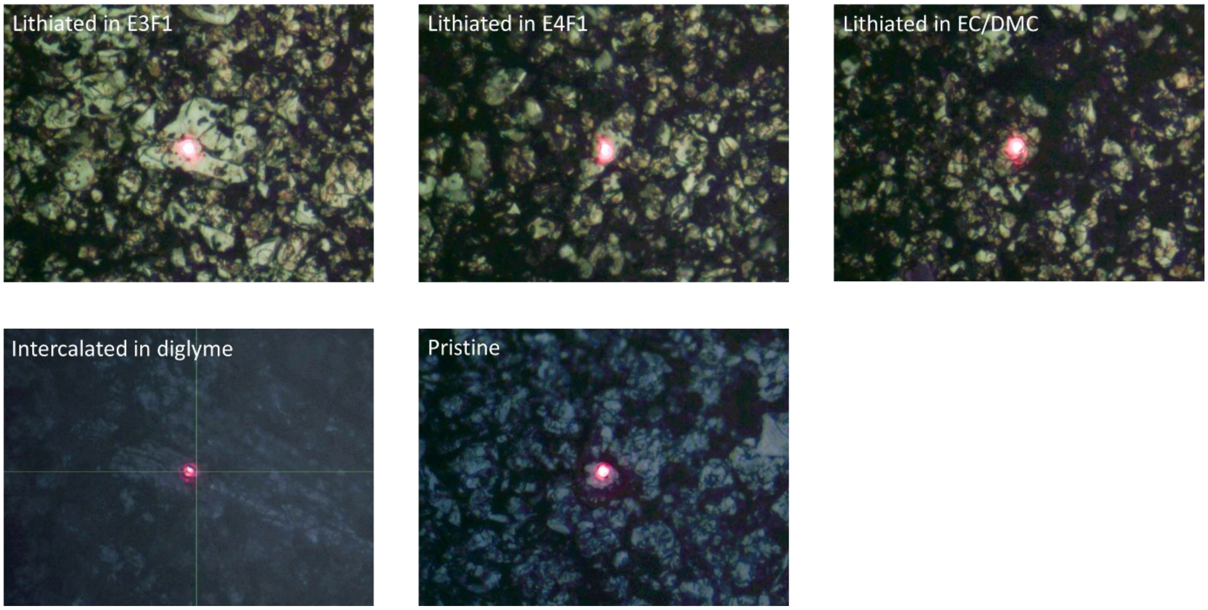

Figure S3. Optical microscopy images (50×) of graphite intercalated in different electrolytes with pristine graphite for comparison. The red dots indicate the position of laser for Raman spectroscopy. Intercalated graphite electrodes were retrieved from Li/Gr cells intercalated to 0.01 V at a rate of C/20 (1 C $\approx$ 2.17 mA cm^{-2}). The graphite intercalated in E3F1, E4F1 and EC/DMC electrolytes have shiny Li_xC_6 particles in golden color. However, graphite intercalated in diglyme electrolyte only has grey colored particles.

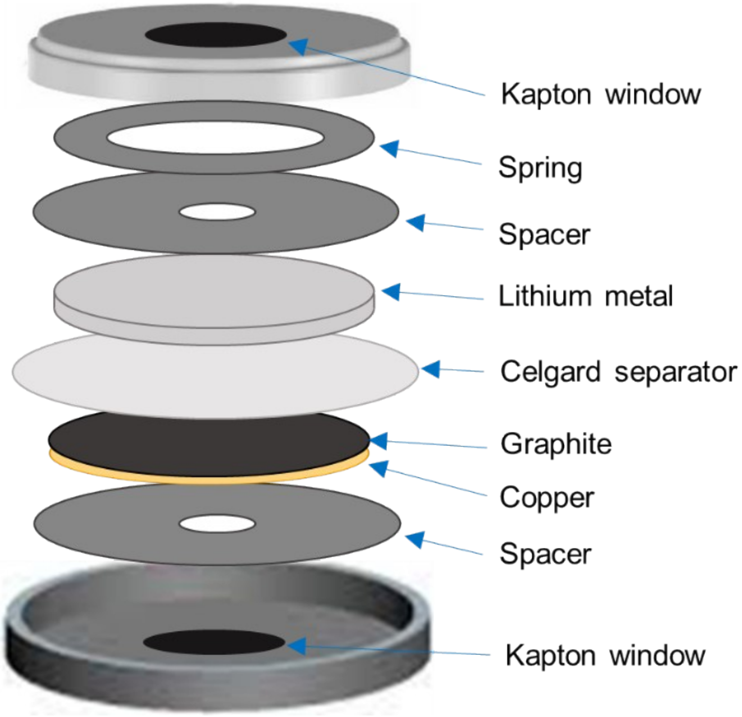

Figure S4. Schematical illustration of coin cell configuration for *in situ* XRD experiment.

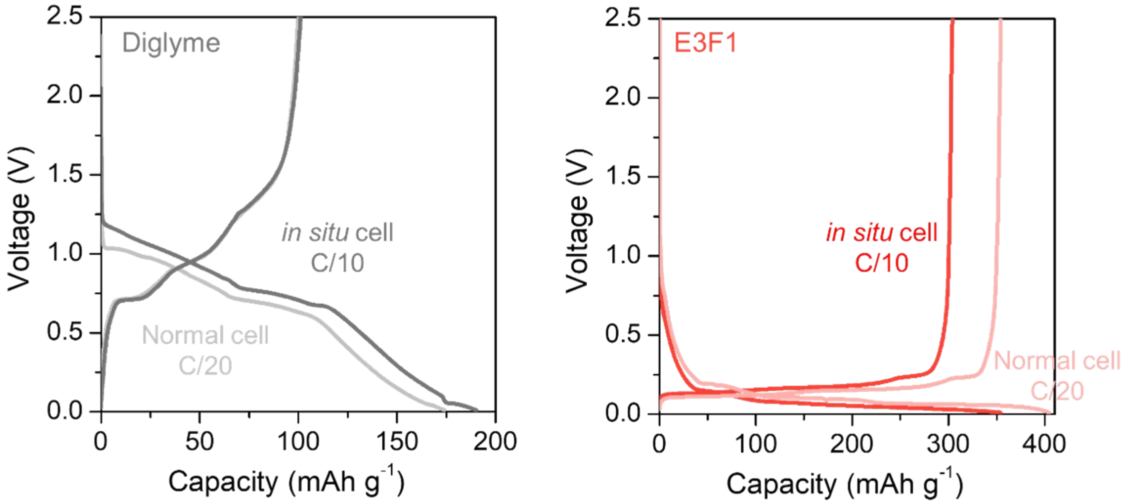

Figure S5. Comparison of *in situ* cells and normal Li/Gr cells using 1 M LiFSA in diglyme and 1 M LiFSA in E3F1 as electrolytes. Voltage profiles of in situ cell mimic normal cells despite minor differences in capacity and overpotential.

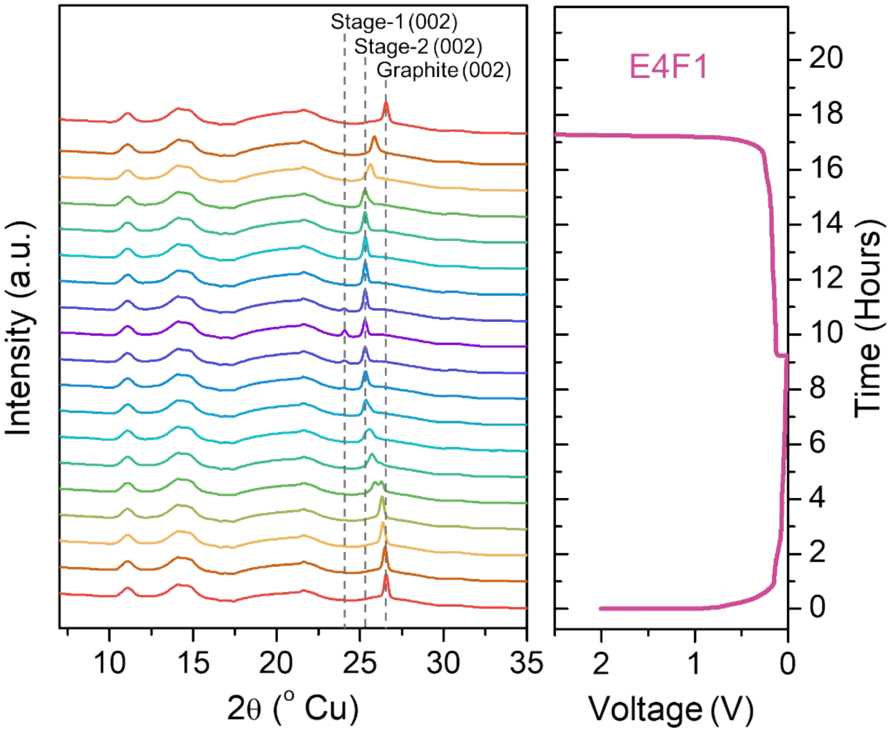

Figure S6. Time-aligned *in situ* XRD patterns and voltage profile of Li/Gr cells using 1 M LiFSA in E4F1 as electrolyte. The *in situ* XRD test results of E4F1 mimic E3F1, indicating both can enable reversible lithium insertion into graphite.

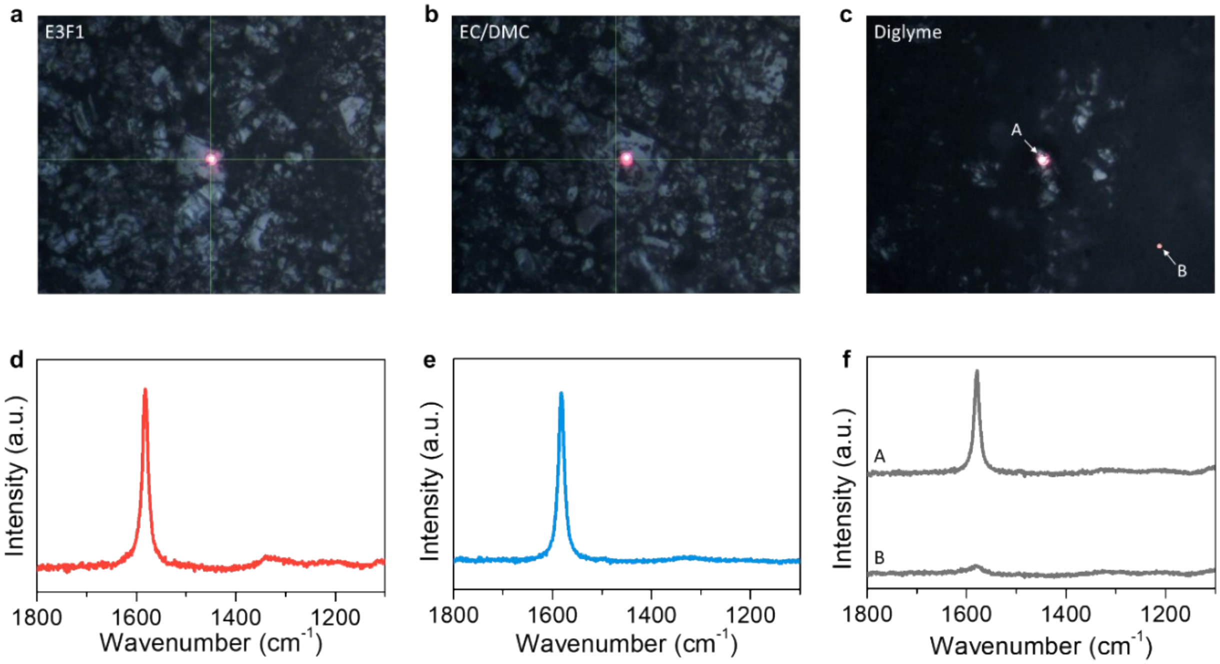

Figure S7. Raman spectra of deintercalated graphite electrodes. **a**-**c**, Optical images (50×) of graphite electrodes cycled in (**a**) E3F1 1 M LiFSA, (**b**) EC/DMC 1 M $LiPF_6$, and (**c**) diglyme 1 M LiFSA. **d**-**f**, Raman spectra of corresponding graphite samples. Raman spectra were collected from the points indicated by red dots except for diglyme sample where Raman spectra of one additional spot is shown. Deintercalated graphite electrodes were retrieved from Gr/LFP cells after three formation cycles (ending on deintercalation) at a current rate of C/20 (1 C ≈ 1.81 mA cm^{-2}).

Discussions: Reflective graphite particles can be observed in the E3F1 and EC/DMC samples in high density and the Raman spectra of those particles exactly mirror pristine graphite, indicating the graphite structure is not altered by cycling. In contrast, optical images show that the diglyme sample only has few reflective graphite particles, and the rest of its surface is dark and rough. Although Raman spectra of such reflective particles still maintain pristine graphite features, the dark regions do not show Raman features for ordered graphite structure. Hence, the structure of most graphite particles has become disordered with cycling in diglyme electrolyte.

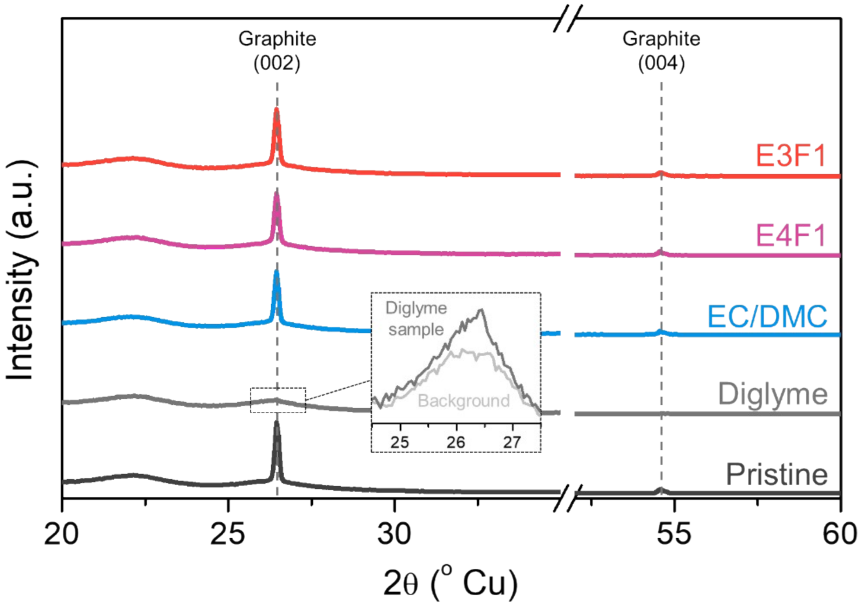

Figure S8. *ex situ* XRD of deintercalated graphite electrodes with pristine graphite for comparison. Inset shows the comparison of diglyme sample with background XRD pattern around graphite (002) peak region. Deintercalated graphite electrodes were retrieved from Gr/LFP cells after three formation cycles (ending on deintercalation) at a current rate of C/20 (1 C ≈ 1.81 mA cm^{-2}).

Discussions: The graphite (002) and (004) peaks are well maintained after cycling in E3F1, E4F1 and EC/DMC electrolytes, indicating reversible graphite structure change with lithium intercalation. By contrast, only a very weak and broad graphite peak can be observed in diglyme sample, which is likely due to exfoliation and disordering of graphite with solvent co-intercalation.

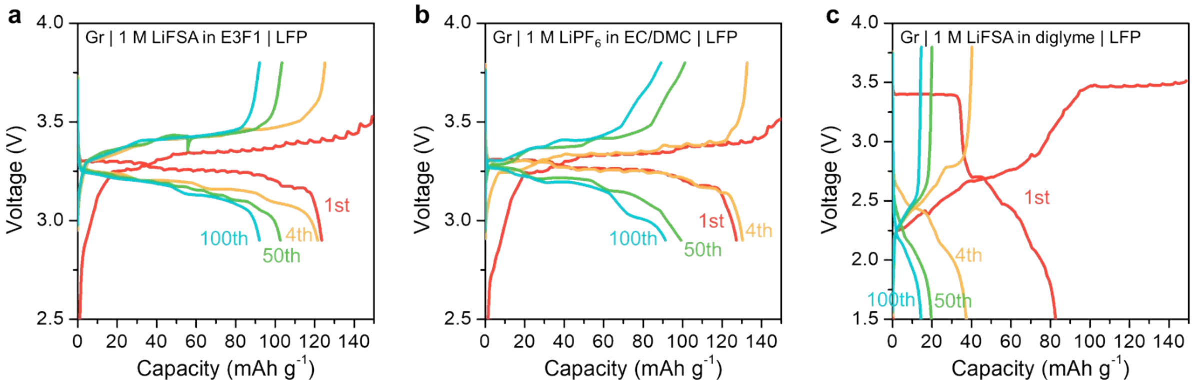

Figure S9. Voltage-capacity plots of graphite/LiFePO$_4$ (Gr/LFP) cells using (**a**) 1 M LiFSA in E3F1, (**b**) 1 M LiPF$_6$ in EC/DMC and (**c**) 1 M LiFSA in diglyme cycled at 20°C. The cells were cycled at a current rate of C/3 after three formation cycles at C/20. (1 C ≈ 1.81 mA cm^{-2})

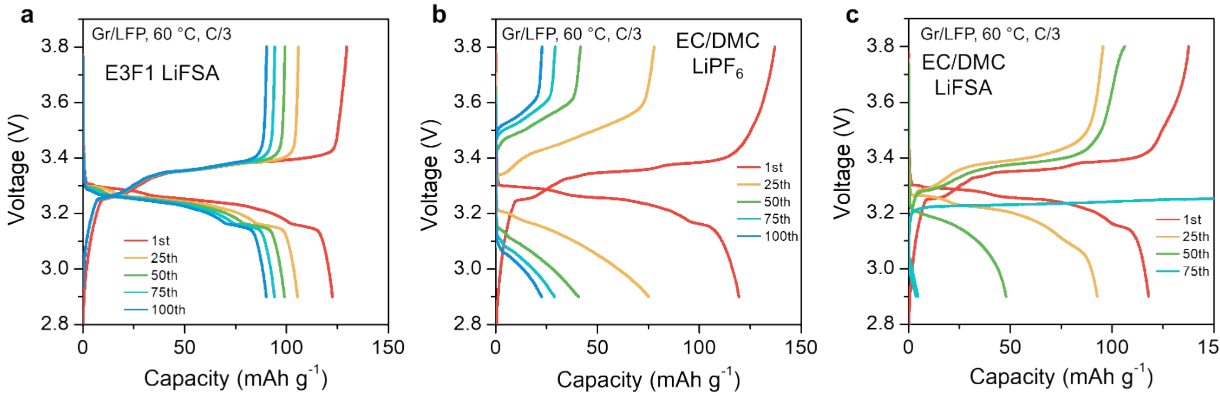

Figure S10. Voltage profiles of graphite/LiFePO$_4$ (Gr/LFP) cells using (**a**) 1 M LiFSA in E3F1, (**b**) 1 M LiPF$_6$ in EC/DMC and (**c**) 1 M LiFSA in EC/DMC at 60°C. The cells were cycled at C/20 three times at 20°C (not shown) prior to 60°C cycling at C/3. (1 C ≈ 1.81 mA cm^{-2})

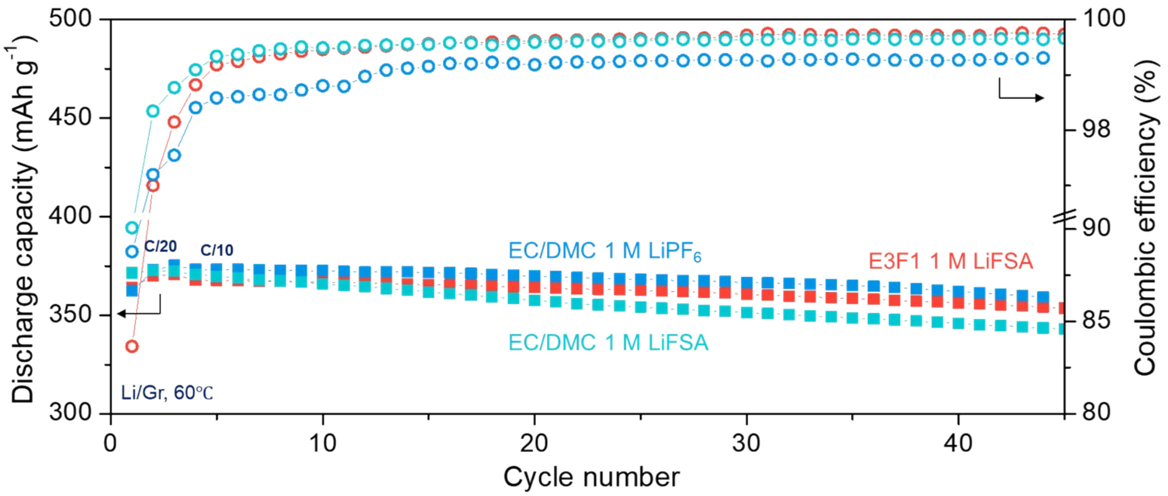

Figure S11. Galvanostatic cycling of lithium metal/graphite (Li/Gr) cells using 1 M LiFSA in E3F1, 1 M $LiPF_6$ in EC/DMC and 1 M LiFSA in EC/DMC as electrolytes. The cells were cycled at 60°C in a current rate of C/10 after three formation cycles at C/20. (1 C ≈ 2.17 mA cm^{-2})

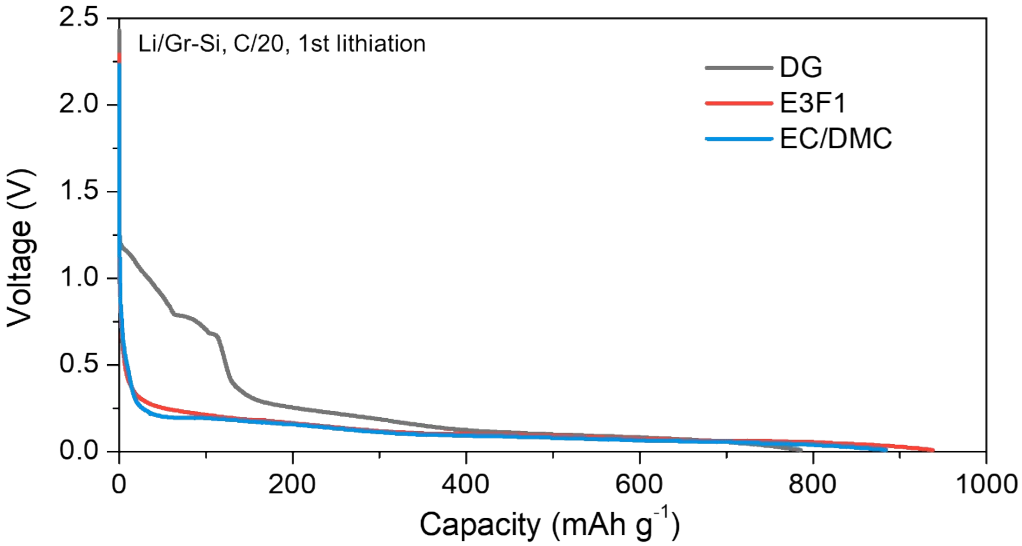

Figure S12. Voltage profile of lithium metal/graphite-silicon (Li/Gr-Si) cells using 1 M LiFSA in E3F1, 1 M LiFSA in diglyme and 1 M $LiPF_6$ in EC/DMC. Li/Gr-Si cells were discharged to a cut-off voltage of 0.01 V at a current rate of C/20 (1 C ≈ 2.83 mA cm^{-2}). Gr-Si electrode overall shows higher specific capacity compared to graphite. E3F1 electrolyte leads to several stable voltage plateaus below 0.3 V that is similar to EC/DMC electrolyte while diglyme cell has a high-voltage (> 0.5 V) plateau at the onset. This indicates the tendency of solvent co-intercalation into graphite is succeeded by Gr-Si composite.

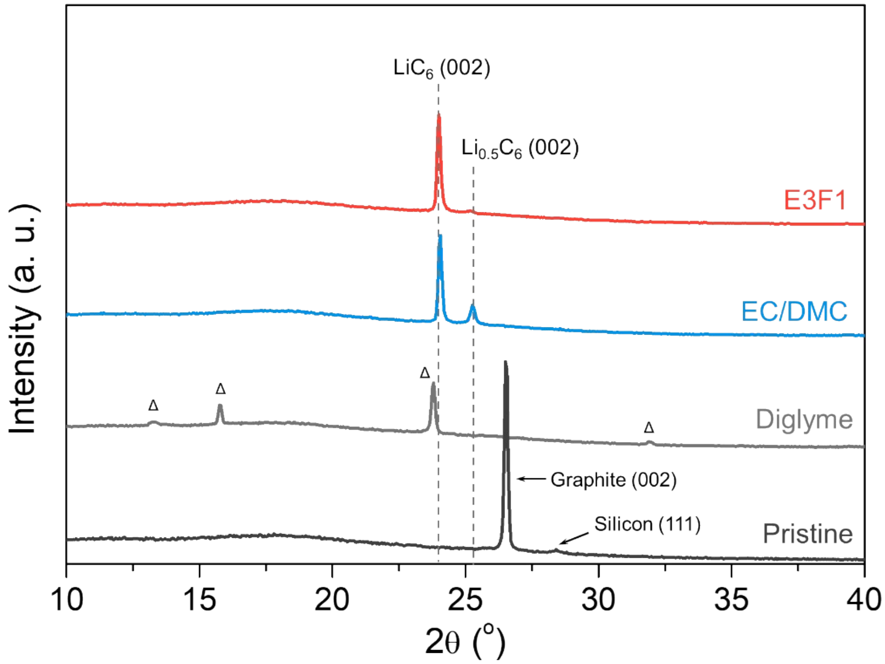

Figure S13. XRD patterns of graphite-silicon (Gr-Si) composite electrode intercalated in E3F1 1 M LiFSA (E3F1), EC/DMC 1 M LiPF$_6$ (EC/DMC) and diglyme 1 M LiFSA (Diglyme) with pristine graphite-silicon composite as control. Δ: (002), (003), (004) and (005) peaks of ternary GIC (from left to right). Intercalated Gr-Si electrodes were prepared in Li/Gr-Si cells by charging to a cut-off voltage of 0.01 V at a current rate of C/20 (1 C ≈ 2.83 mA cm^{-2}).

Discussions: The graphite XRD peaks of intercalated Gr-Si composition mirror intercalated graphite electrode (Fig. 3a) for each specific electrolyte. This indicates the intercalation mechanism into graphite is not altered by compositing with silicon. The silicon (111) peak of pristine Gr-Si electrode disappears after lithiation for all electrolytes tested, which agrees with literatures that the lithiation of silicon leads to amorphous lithium-silicon alloy at room temperature.[5]

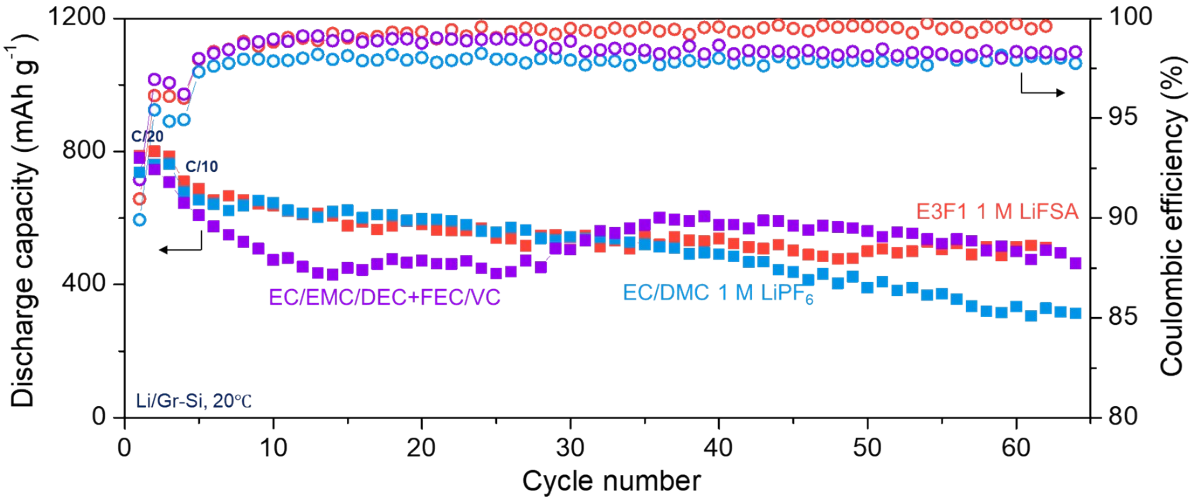

Figure S14. Galvanostatic cycling of lithium metal/graphite-silicon (Li/Gr-Si) cells using 1 M LiFSA in E3F1, 1 M $LiPF_6$ in EC/DMC and 1.2 M $LiPF_6$ in EC/EMC/DEC+2% FEC+1%VC (EC/EMC/DEC+FEC/VC) as electrolytes. The cells were cycled at 20°C at a current rate of C/10 after three formation cycles at C/20. (1 C ≈ 2.83 mA cm^{-2})

Discussions: Despite some fluctuation, all three electrolytes can maintain a discharge capacity of ~ 600 mAh g^{-1} in the long term cycling of Li/Gr-Si cells. E3F1 show significantly higher Coulombic efficiency (~99.5% around 50th cycle) than EC/DMC (~97.9% around 50th cycle) or EC/EMC/DEC+FEC/VC (~98.2% around 50th cycle) at the later cycles. This indicates E3F1 has less parasitic reaction with Gr-Si electrode, which corroborates the Gr-Si/LFP full cell cycling results shown in Fig. 5c.

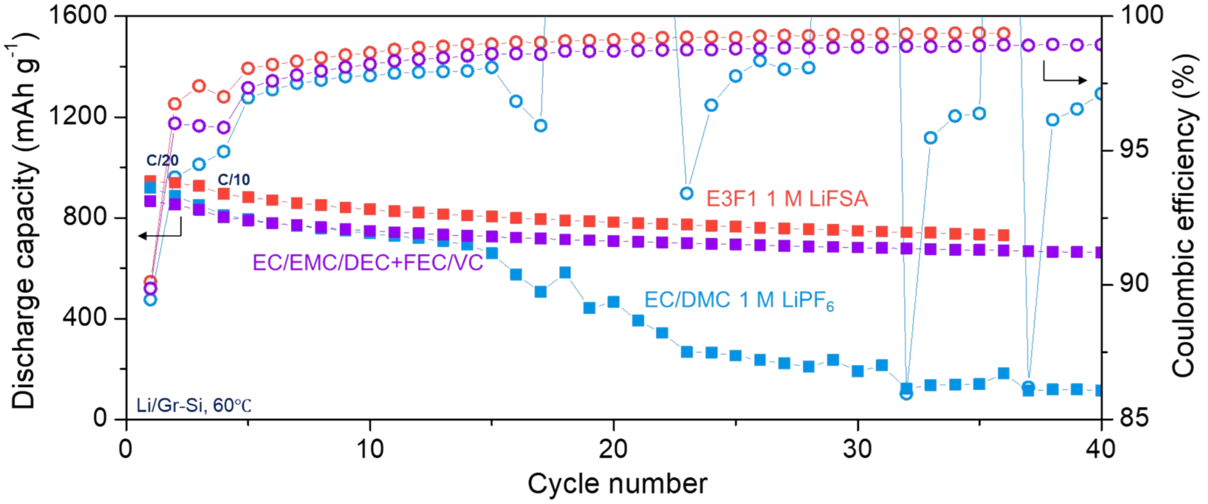

Figure S15. Galvanostatic cycling of lithium metal/graphite-silicon (Li/Gr-Si) cells using 1 M LiFSA in E3F1, 1 M LiPF$_6$ in EC/DMC and 1.2 M LiPF$_6$ in EC/EMC/DEC+2% FEC+1%VC (EC/EMC/DEC+FEC/VC) as electrolytes at 60°C. The cells were cycled at 60°C in a current rate of C/10 after three formation cycles at C/20. (1 C ≈ 2.83 mA cm^{-2})

Discussions: When Li/Gr-Si cells are cycled at 60°C, higher specific capacity (~800 mAh g^{-1}) of Gr-Si electrode is achieved likely due to better kinetics. With growing cycle number, the Coulombic efficiency of E3F1 cell gradually stabilizes around 99.3%, which is even higher than room temperature and supports the superior thermal stability of E3F1. In contrast, the EC/DMC cell shows rapid capacity decay after 14th cycle due to its poor thermal stability. The EC/EMC/DEC+FEC/VC electrolyte shows better thermal stability than EC/DMC LiPF$_6$ but its Coulombic efficiency is still lower than E3F1 electrolyte.

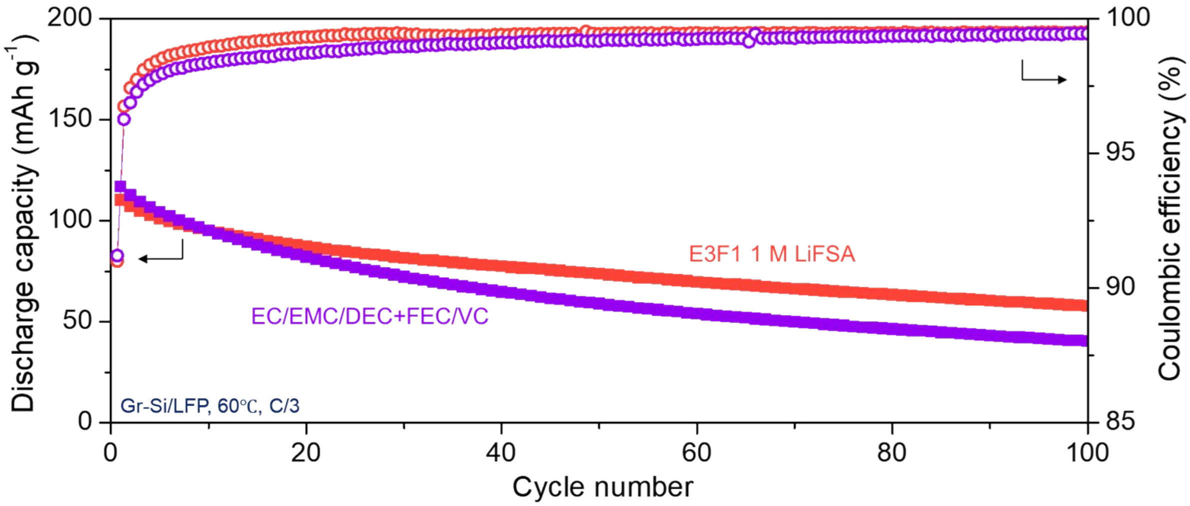

Figure S16. Galvanostatic cycling of graphite-silicon/$LiFePO_4$ (Gr-Si/LFP) cells using 1 M LiFSA in E3F1 and 1.2 M $LiPF_6$ in EC/EMC/DEC+2% FEC+1%VC (EC/EMC/DEC+FEC/VC) as electrolytes at 60°C. Three formation cycles at C/20 were performed at 20°C (not shown) prior to 60°C cycling. (1 C $\approx$ 1.81 mA cm^{-2}, N/P $\approx$ 1.2)

Discussions: Gr-Si/LFP cells cycled at 60℃ show similar cycling performance trend as 20℃ cycling, where E3F1 has higher Coulombic efficiency and better capacity retention than EC/EMC/DEC+FEC/VC. E3F1 electrolyte keeps high Coulombic efficiency at 60℃ with capacity retention comparable to 20℃ (57.8 mAh g^{-1} versus 70.3 mAh g^{-1} at the 100th cycle). The cycling of Gr-Si based cells at 60℃ proves that the superior thermal stability of E3F1 is not dependent on battery chemistry.

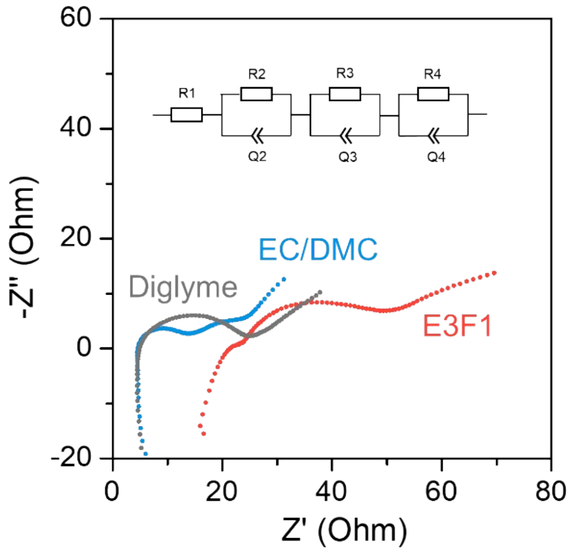

Figure S17. Electrochemical impedance spectra (EIS) of graphite/LiFePO$_4$ (Gr/LFP) cells using 1 M LiPF$_6$ in EC/DMC, 1 M LiFSA in E3F1 and 1 M LiFSA in diglyme as electrolytes after three formation cycles at C/20. Inset shows the equivalent circuit used for fitting.

Table S1 | Fitting parameters of EIS

	Ohmic Resistance	Double Layer Components			SEI Components			Charge Transfer Components		
	R1 (Ω)	**R2 (Ω)**	**Q2 (F s^{a-1})**	**a2**	**R3 (Ω)**	**Q3 (F s^{a-1})**	**a3**	**R4 (Ω)**	**Q4 (F s^{a-1})**	**a4**
E3F1	20.34	4.09	2.76×10^{-3}	0.30	21.88	1.26×10^{-3}	0.74	70.97	1.01×10^{-2}	0.50
EC/DMC	4.48	7.02	9.67×10^{-6}	0.92	16.12	4.15×10^{-3}	0.54	68.4	1.80×10^{-2}	0.81
Diglyme	4.80	7.12	1.16×10^{-3}	0.54	13.89	6.14×10^{-6}	0.82	78.95	1.99×10^{-3}	0.53

Discussions: LFP was selected instead of lithium metal to minimize the influence of counter electrode because most electrolytes do not form resistive passivation layers at the interface with LFP.[1,2] Fig. S17 and Table S1 show that E3F1 have higher interfacial resistance (21.88 Ω), which supports the formation of SEI in fluoroether electrolytes. On the contrary, the diglyme cell has lower interfacial resistance (13.89 Ω). The lack of SEI in the diglyme cell could be explained by two observations: First, the solvent co-intercalation reaction starts at a much higher potential than normal lithiation reaction (1.24 V vs 0.19 V); Secondly, glyme ether solvents are known for their good reductive stabilities and are not reduced to form a robust SEI.[3] Kim et al. also reported the absence of a passivation layer at the interface of glyme electrolytes and graphite electrode using transmission electron microscopy (TEM).[4]

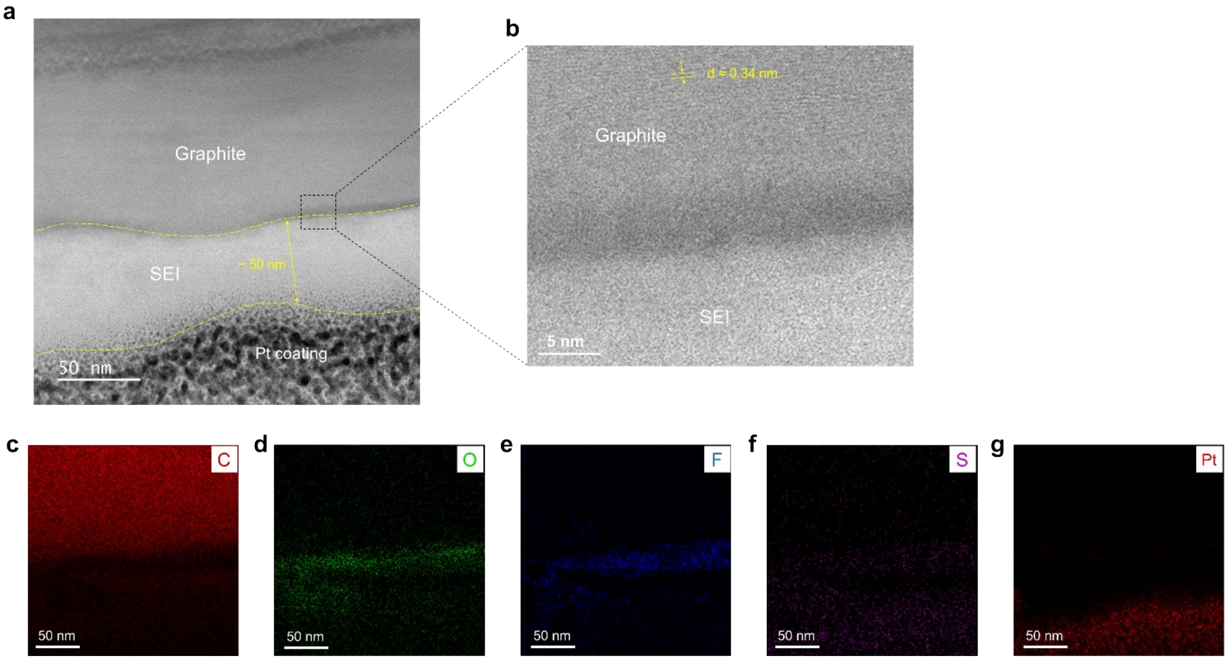

Figure S18. **a**, Transmission electron microscopy (TEM) image of graphite SEI formed in E3F1 1 M LiFSA electrolyte. **b**, Magnified view of the interface between graphite and SEI. **c**-**g**, Energy-dispersive X-ray spectroscopy (EDS) mapping of the region shown in (**a**).

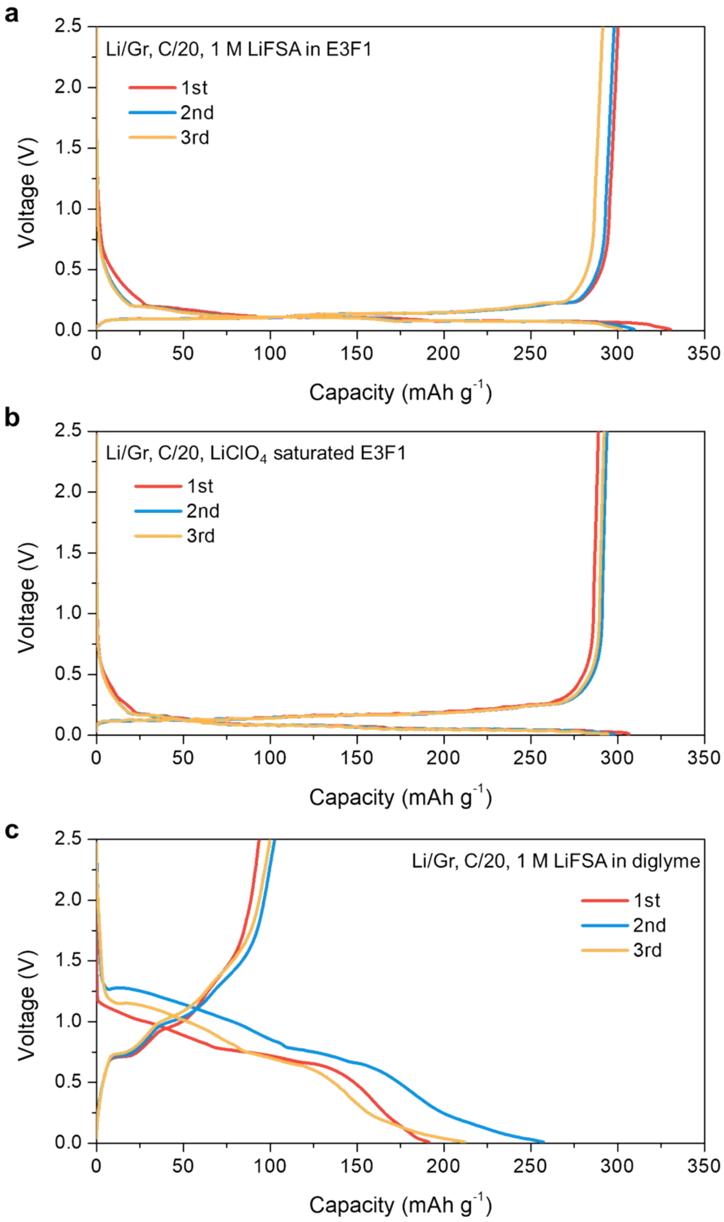

Figure S19. Voltage profile of Li/Gr (graphite electrode using SBR binder) cells using (**a**) 1 M LiFSA in E3F1, (**b**) $LiClO_4$ saturated E3F1 and (**c**) 1 M LiFSA in diglyme as electrolytes. Li/Gr cells were cycled at a current rate of C/20 (1 C ≈ 0.8 mA cm^{-2}) three times before XPS characterization.

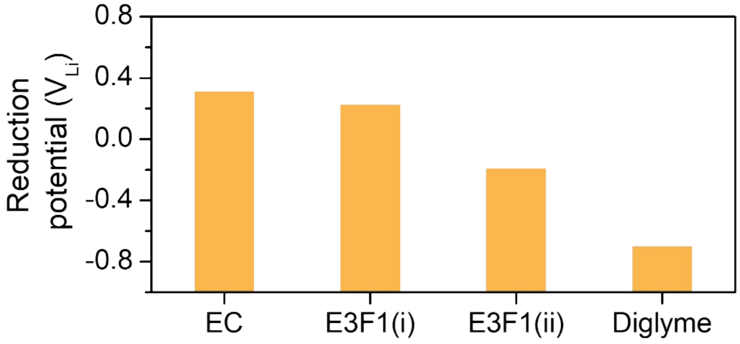

Figure S20. Adiabatic reduction potentials of electrolyte solvents predicted by density functional theory (DFT) calculations (V_{Li}: volts referenced to Li/Li^+ electrode).

Discussions: Adiabatic reduction potential is defined as the electrochemical potential of single electron reduction ($M + e^- \rightarrow M^-$), where the geometry of product (M^-) is optimized. EC has a calculated reduction potential of 0.31 V_{Li}, which is above the potential of graphite lithiation reaction (~ 0 V_{Li}). It is widely accepted that the reductive degradation of EC leads to surface passivation of graphite anode.[6,7] In contrast, diglyme shows a much lower reduction potential of –0.70 V_{Li}, indicating diglyme molecules are thermodynamically more stable at the operation potential of the graphite electrode. The good reductive stability of diglyme explains its deficiency in passivating the graphite electrode. After fluorination, the reductive potential of E3F1 increases to 0.22 V_{Li} and −0.19 V_{Li} based on different degradation pathways. The reductive degradation of E3F1 allows for graphite electrode passivation and enables reversible lithium (de)intercalation. Similar effects of fluorination have been widely reported for other fluorinated ether and carbonate solvents in lithium metal batteries.[8–11] Fig. 6e shows that the cleavage of the C−F bond (i) is the most favorable reduction pathway of E3F1 and is responsible for its positive reduction potential, but the cleavage of C−O bond (ii) is also possible since it leads to a reduction potential close to 0 V_{Li}.

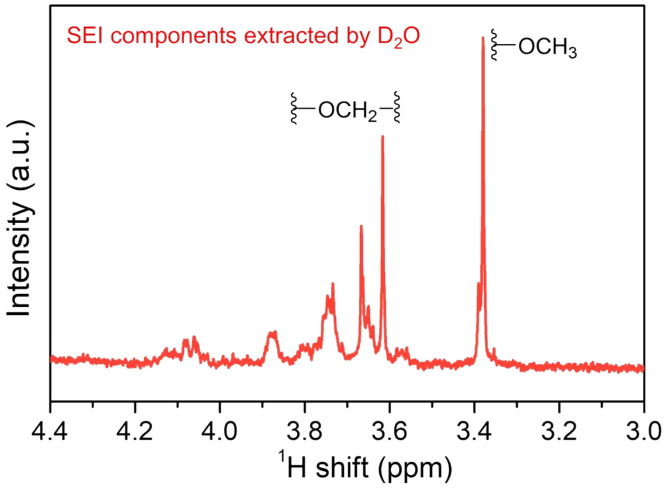

Figure S21. ^{1}H NMR spectra of E3F1-derived SEI components dissolved in D_2O. The peaks between 4.2 ppm and 3.6 ppm are assigned to $-OCH_2-$ groups in different chemical environments and the peaks around 3.4 ppm are assigned to $-OCH_3$ groups.

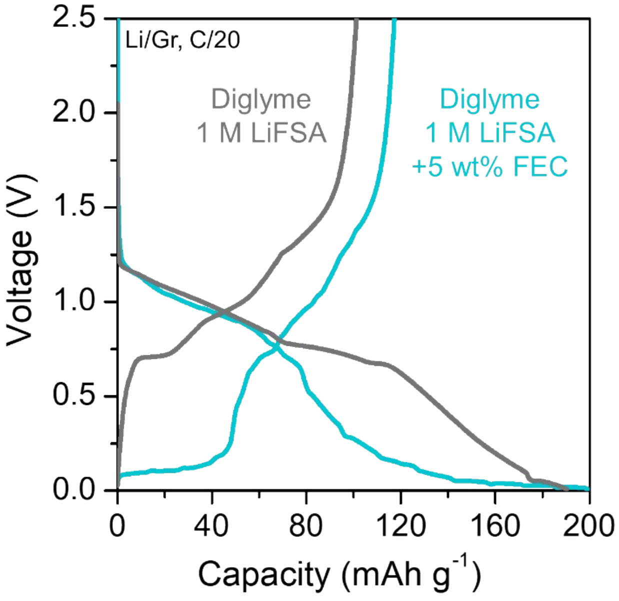

Figure S22. The first cycle of Li/Gr half cells using 1 M LiFSA in diglyme and 1 M LiFSA in diglyme with 5 wt% FEC. The addition of “SEI former” such as FEC does not suppress the co-intercalation of diglyme.

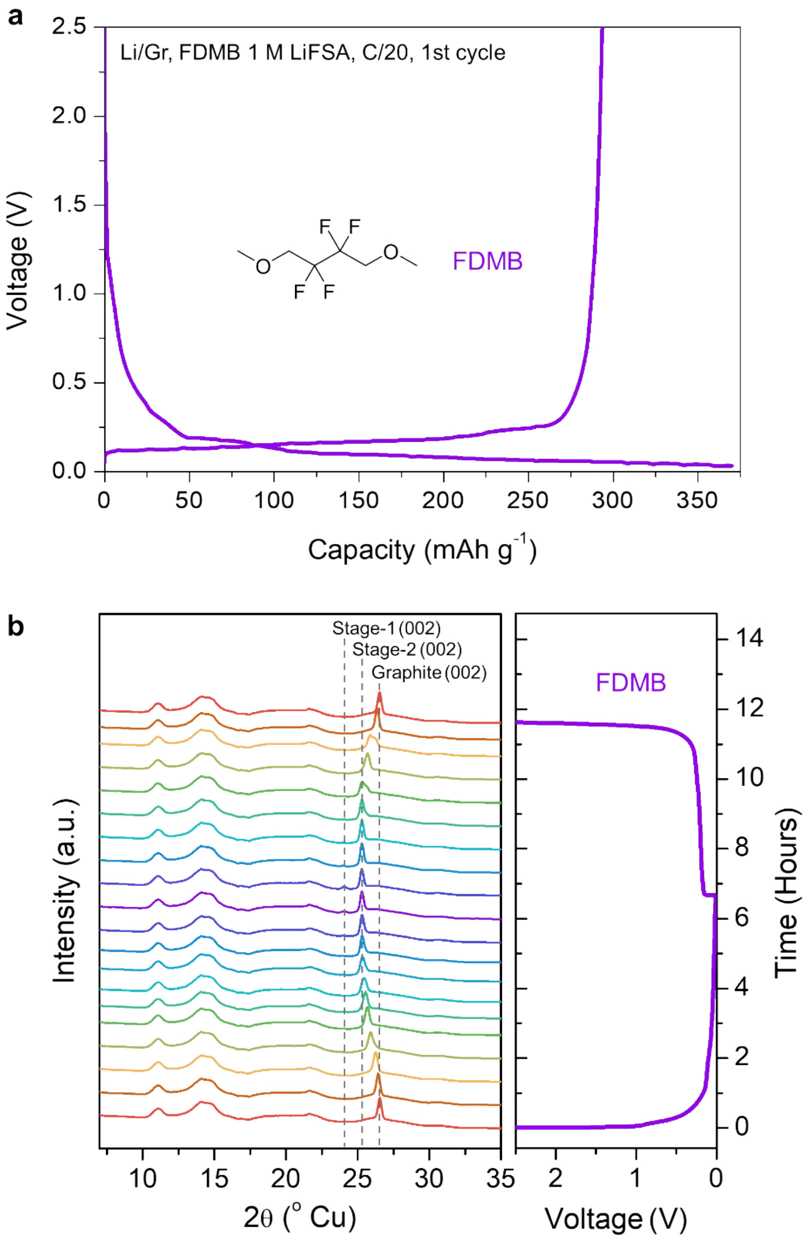

Figure S23. **a**, Galvanostatic cycling of the Li/Gr cell using 1 M LiFSA in FDMB[12] as electrolyte. **b**, Time-aligned *in situ* XRD patterns and voltage profiles of Li/Gr cells using 1 M LiFSA in FDMB as electrolyte. Both the voltage profile of the Li/Gr cell and *in situ* XRD results indicate FDMB electrolyte can also enable reversible lithium intercalation into graphite without solvent co-intercalation.

References

(1) Cuisinier, M.; Dupré, N.; Martin, J.-F.; Kanno, R.; Guyomard, D. Evolution of the LiFePO4 Positive Electrode Interface along Cycling Monitored by MAS NMR. *J. Power Sources* **2013**, *224*, 50–58. https://doi.org/https://doi.org/10.1016/j.jpowsour.2012.08.099.

(2) Edström, K.; Gustafsson, T.; Thomas, J. O. The Cathode–Electrolyte Interface in the Li-Ion Battery. *Electrochim. Acta* **2004**, *50* (2), 397–403. https://doi.org/https://doi.org/10.1016/j.electacta.2004.03.049.

(3) Feng, S.; Chen, M.; Giordano, L.; Huang, M.; Zhang, W.; Amanchukwu, C. V; Anandakathir, R.; Shao-Horn, Y.; Johnson, J. A. Mapping a Stable Solvent Structure Landscape for Aprotic Li–Air Battery Organic Electrolytes. *J. Mater. Chem. A* **2017**, *5* (45), 23987–23998. https://doi.org/10.1039/C7TA08321A.

(4) Kim, H.; Lim, K.; Yoon, G.; Park, J.-H.; Ku, K.; Lim, H.-D.; Sung, Y.-E.; Kang, K. Exploiting Lithium–Ether Co-Intercalation in Graphite for High-Power Lithium-Ion Batteries. *Adv. Energy Mater.* **2017**, *7* (19), 1700418. https://doi.org/https://doi.org/10.1002/aenm.201700418.

(5) Huggins, R. A. Lithium Alloy Negative Electrodes. *J. Power Sources* **1999**, *81–82*, 13–19. https://doi.org/https://doi.org/10.1016/S0378-7753(99)00124-X.

(6) Nie, M.; Chalasani, D.; Abraham, D. P.; Chen, Y.; Bose, A.; Lucht, B. L. Lithium Ion Battery Graphite Solid Electrolyte Interphase Revealed by Microscopy and Spectroscopy. *J. Phys. Chem. C* **2013**, *117* (3), 1257–1267. https://doi.org/10.1021/jp3118055.

(7) Xu, K. Whether EC and PC Differ in Interphasial Chemistry on Graphitic Anode and How. *J. Electrochem. Soc.* **2009**, *156* (9), A751. https://doi.org/10.1149/1.3166182.

(8) Park, S.-J.; Hwang, J.-Y.; Yoon, C. S.; Jung, H.-G.; Sun, Y.-K. Stabilization of Lithium-Metal Batteries Based on the in Situ Formation of a Stable Solid Electrolyte Interphase Layer. *ACS Appl. Mater. Interfaces* **2018**, *10* (21), 17985–17993. https://doi.org/10.1021/acsami.8b04592.

(9) Zhang, X.-Q.; Cheng, X.-B.; Chen, X.; Yan, C.; Zhang, Q. Fluoroethylene Carbonate Additives to Render Uniform Li Deposits in Lithium Metal Batteries. *Adv. Funct. Mater.*

2017, *27* (10), 1605989. https://doi.org/10.1002/adfm.201605989.

(10) Zhang, Z.; Hu, L.; Wu, H.; Weng, W.; Koh, M.; Redfern, P. C.; Curtiss, L. A.; Amine, K. Fluorinated Electrolytes for 5 V Lithium-Ion Battery Chemistry. *Energy Environ. Sci.* **2013**, *6* (6), 1806–1810. https://doi.org/10.1039/C3EE24414H.

(11) Cao, X.; Ren, X.; Zou, L.; Engelhard, M. H.; Huang, W.; Wang, H.; Matthews, B. E.; Lee, H.; Niu, C.; Arey, B. W.; Cui, Y.; Wang, C.; Xiao, J.; Liu, J.; Xu, W.; Zhang, J.-G. Monolithic Solid-Electrolyte Interphases Formed in Fluorinated Orthoformate-Based Electrolytes Minimize Li Depletion and Pulverization. *Nat. Energy*. https://doi.org/10.1038/s41560-019-0464-5.

(12) Yu, Z.; Wang, H.; Kong, X.; Huang, W.; Tsao, Y.; Mackanic, D. G.; Wang, K.; Wang, X.; Huang, W.; Choudhury, S.; Zheng, Y.; Amanchukwu, C. V; Hung, S. T.; Ma, Y.; Lomeli, E. G.; Qin, J.; Cui, Y.; Bao, Z. Molecular Design for Electrolyte Solvents Enabling Energy-Dense and Long-Cycling Lithium Metal Batteries. *Nat. Energy* **2020**, *5*, 526–533. https://doi.org/10.1038/s41560-020-0634-5.